A MULTISCALE MODELING METHOD FOR DEFORMATIONS ON ATOMIC LATTICE DEFECTS AND APPLICATION TO PLASTICITY

Peter W. Chung* and John D. Clayton

U.S. Army Research Laboratory, Aberdeen Proving Ground, MD 21005

ABSTRACT

Computing the displacements of atoms undergoing deformation in a perfect lattice requires the use of the so-called Cauchy-Born approximation. Near defects such as at vacancies or dislocations, this approximation does not hold and a computationally costly energy minimization over a large number of atoms is unavoidable. Presented is a self-consistent multiscale methodology enabling an approximation to the displacements near defects without requiring full energy minimization over successive load increments. It enables description of the fundamental mechanical behavior of crystalline materials at the length scale of a macroscopic continuum (i.e., millimeter resolution) given discrete atomic interactions at the nanoscale (i.e., angstrom resolution). The basic formulation is derived from mathematical homogenization which requires the definition of a representative crystalline volume element containing periodic defects. Numerical simulations demonstrate the utility of the framework for the particular case of tungsten. Elastic stiffness and energetic properties of periodic unit cells containing vacancies, screw dislocations, and low-angle twist boundaries are computed followed by demonstrative calculations of the extension to atomistic plastic flow.

1. INTRODUCTION

In the field of solid mechanics, one of the key impetuses for multiscale modeling is to reduce the empiricism of constitutive models to an irreducible level. Typically, this is the level of atomistic interactions. The postulated benefits of such a reduction are numerous. All continuum phenomenology would be intrinsic to the atomistic interaction energy either in terms of quasistatic atomic forces or through the small atomic vibration periods (femtoseconds). Moreover, no assumption of domain simple connectedness would be required so that materials may develop internal interfaces or sliding boundaries naturally.

In progressing towards these benefits, atomistic-to-continuum scale multiscale techniques continue to enjoy strong consideration for modeling nanoscopic structures that are difficult to treat with atomistics alone (Tadmor et al., 1996; Rudd & Broughton, 2001; Ghoniem et al., 2003). With the ever increasing power of microprocessors, one might eschew multiscale methods and instead pursue brute force large-scale atomistic calculations (cf. Seppälä et al., 2004) to evoke continuum behavior. However, at the current rate of increase in performance, many years still remain before computers will be capable of simulating the response of enough atoms, over a time scale of sufficient duration to realistically address design of "engineer-able" materials.

Despite the successes of atomistic-to-continuum modeling methods, significant limitations still remain. Most notable among these is the requirement of kinematic approximations on deforming crystals that preclude multiscale methods from handling important solid mechanics problems in general electromagnetic materials (Cole, et al., 2003). The kinematic approximation, also called the Cauchy-Born rule (cf. Ericksen, 1984), reduces the number of computational degrees of freedom by approximating the displacements of lattice points through affine maps using the deformation gradient. As a mathematical tool for multiscale modeling, the Cauchy-Born rule is indispensable as it unifies the behavior of all atoms in a perfect crystal, effectively enabling the replacement of many atom degrees of freedom with a single second rank tensor. Crystals that are amenable to the Cauchy-Born approximation are typically monocrystalline, covalent, or centrosymmetric.

For imperfect crystals, or more specifically crystals that lack an axis of inversion symmetry (Ericksen, 1984), no similar approximation currently exists. These types of crystals usually are complex, ionic, or contain lattice defects. Most engineered materials, particularly of interest to the Army and long-term commercial application, contain critical components whose crystals are of this type.

In this paper, we develop a numerical method to enable multiscale modeling of imperfect crystals. The method is based on but computationally less expensive than an asymptotic homogenization technique developed earlier by the authors for hyperelastic semiconductor crystals (Chung & Namburu, 2003; Chung, 2004). We demonstrate its use for zero temperature mechanics of a crystalline transition metal solid with comparisons to direct molecular static results. Under strain, we examine point, line and plane defects. Additionally, we present initial results for the extension of the method to handle bulk plasticity using only the atomistic information for the constitutive properties through the introduction of an evolving reference configuration.

The solid mechanical properties of interest are the effective elastic stiffness and strain energy density.

1. REPORT DATE **01 NOV 2006**	2. REPORT TYPE **N/A**	3. DATES COVERED **-**

4. TITLE AND SUBTITLE	5a. CONTRACT NUMBER
A Multiscale Modeling Method for Deformations on Atomic Lattice Defects and Application to Plasticity	5b. GRANT NUMBER
	5c. PROGRAM ELEMENT NUMBER

6. AUTHOR(S)	5d. PROJECT NUMBER
	5e. TASK NUMBER
	5f. WORK UNIT NUMBER

7. PERFORMING ORGANIZATION NAME(S) AND ADDRESS(ES) **U.S. Army Research Laboratory, Aberdeen Proving Ground, MD 21005**	8. PERFORMING ORGANIZATION REPORT NUMBER

9. SPONSORING/MONITORING AGENCY NAME(S) AND ADDRESS(ES)	10. SPONSOR/MONITOR'S ACRONYM(S)
	11. SPONSOR/MONITOR'S REPORT NUMBER(S)

12. DISTRIBUTION/AVAILABILITY STATEMENT
Approved for public release, distribution unlimited

13. SUPPLEMENTARY NOTES
See also ADM002075., The original document contains color images.

14. ABSTRACT

15. SUBJECT TERMS

16. SECURITY CLASSIFICATION OF:			17. LIMITATION OF ABSTRACT **UU**	18. NUMBER OF PAGES **26**	19a. NAME OF RESPONSIBLE PERSON
a. REPORT **unclassified**	b. ABSTRACT **unclassified**	c. THIS PAGE **unclassified**			

Section 2 overviews the multiscale homogenization equations applicable to nonlinear hyperelastic problems. Section 3 introduces the notion of discrete atoms in the context of homogenization. This approach is extended to numerous periodic defect examples in Section 4, followed by discussions and conclusions in Section 5.

2. MATHEMATICAL DEVELOPMENTS

2.1 Governing equations

Two-scale homogenization involves the self-consistent solution of two coupled equations derived from the statement of conservation of linear momentum. In brief, for a given energy density Ψ in reference configuration B_0, current configuration B at time t, with reference macroscopic coordinates X and current coordinates $x^a = x^a(X^A, t)$, the respective microscopic coordinates Y and $y^a = y^a(Y^A, t)$, coarse- and fine-scale displacements $\mathbf{u}$ and $\mathbf{v}$, the corresponding macroscopic and microscopic deformation gradients $F_{.A}^a = \partial u^a / \partial X^A + \delta_{.A}^a$ and $f_{.A}^a = \partial y^a / \partial Y^A + \delta_{.A}^a$, and the assumption of additive decomposition of displacements $u^a = \overline{u}^a + \tilde{u}^a = \overline{u}^a + \varepsilon \tilde{v}^a$ (Chung, 2004), we have

$$\frac{1}{Y} \int_Y \int_V \frac{\partial \Psi}{\partial F_{.B}^a} \frac{\partial (\delta \overline{u}^a)}{\partial X^B} dVdY = \int_{\partial V} T^a g_{ab} \delta \overline{u}^b dA \qquad (1)$$
$$+ \int_V B^a g_{ab} \delta \overline{u}^b dV, \qquad \left(\forall \delta \overline{u}^a \right)$$

$$\frac{1}{Y} \int_Y \int_V \frac{\partial \Psi}{\partial F_{.B}^a} \frac{\partial (\delta \tilde{v}^a)}{\partial Y^B} dVdY = 0. \qquad \left(\forall \delta \tilde{v}^a \right) \qquad (2)$$

This set of equations defines conventional quasistatic asymptotic homogenization. The coarse-scale Eq. (1) and fine-scale Eq. (2) are coupled through the constitutive dependency $\Psi = \Psi \left(\mathbf{F} \left(\partial \overline{\mathbf{u}} / \partial \mathbf{X}, \partial \tilde{\mathbf{v}} / \partial \mathbf{Y} \right) \right)$.

In equations (1) and (2), $\overline{u}^a$ represents the displacement that would exist in a microscopically homogeneous medium and $\tilde{u}^a$ accounts for fine-scale heterogeneity, with corresponding fine-scale representation $\tilde{v}^a$. The corresponding microscopic decomposition is

$$v^a = \varepsilon^{-1} u^a = \overline{v}^a + \tilde{v}^a = \left(F_{.A}^a - \delta_{.A}^a \right) Y^A + \tilde{v}^a, \qquad (3)$$

with $\overline{v}^a$ the microscopic displacement arising from the projection to the fine-scale of the macroscopic deformation gradient $F_{.A}^a$. From here we may write the decomposition

$$F_{.A}^a = \frac{\partial \overline{u}^a}{\partial X^A} + \frac{\partial \tilde{v}^a}{\partial Y^A} + \delta_{.A}^a = \left(\frac{\partial \overline{u}^a}{\partial X^A} \delta_{.\overline{\alpha}}^A + \delta_{.\overline{\alpha}}^a \right) \tilde{F}_{.A}^{\overline{\alpha}} = \overline{F}_{.\overline{\alpha}}^a \tilde{F}_{.A}^{\overline{\alpha}} , \quad (4)$$

where $\overline{F}_{.\overline{\alpha}}^a$ is the deformation gradient under microscopically homogeneous conditions and $\tilde{F}_{.A}^{\overline{\alpha}} = \overline{F}_{.a}^{-1\overline{\alpha}} F_{.A}^a$ depends upon the gradient of $\tilde{v}$ and thus accounts for heterogeneity due to defect fields. Barred Greek indices denote a third configuration $\overline{B}$ for the material associated with the multiplicative decomposition in the last of (4).

2.2 Homogenization with an evolving intermediate frame

Consider now a continuum elastic-plastic material where the deformation gradient $\mathbf{F}$ is decomposed into a lattice part, $\mathbf{F^L}$, and a plastic part, $\mathbf{F^P}$ (Bilby et al., 1957; Teodosiu, 1969):

$$\mathbf{F} = \mathbf{F^L}\mathbf{F^P} , \qquad F = F_{\alpha}^{La} F_{.A}^{P\alpha} . \qquad (5)$$

This presumes the existence of an intermediate configuration $\tilde{B}$, with $\mathbf{F^P}$ the tangent mapping between B_0 and $\tilde{B}$, and $\mathbf{F^L}$ the tangent mapping from $\tilde{B}$ to B. The plastic map $\mathbf{F^P}$ reflects contributions to the total deformation that leave the lattice unperturbed, such as the flux of mobile dislocations. The lattice map $\mathbf{F^L}$ includes all other kinematic contributions, including rigid body motions, elastic fields, and residual elastic fields attributed to the lattice defects.

2.3 Plasticity

In an elastic-plastic body, it is typically assumed that the free energy depends only upon that part of the deformation that affects the lattice, in other words,

$$\tilde{\Psi} = J^{P-1} \Psi(\mathbf{F}, \mathbf{F^P}, \tilde{\boldsymbol{\xi}}, \theta) = \tilde{\Psi}(\mathbf{F^L}, \tilde{\boldsymbol{\xi}}, \theta), \qquad (6)$$

where $\tilde{\Psi}$ is measured per unit intermediate volume on $\tilde{B}$, and where we have also included the dependence of the free energy on absolute temperature θ. Additionally, $\tilde{\boldsymbol{\xi}}$ is a vector of internal state variables accounting for deviations in stored energy from that of a perfect lattice. Notice that generally, $\mathbf{F^L}$ and $\mathbf{F^P}$ of Eq. (5) and $\overline{\mathbf{F}}$ and $\tilde{\mathbf{F}}$ of Eq. (4) are four distinct deformation mappings, with corresponding configurations of the body depicted in Fig. 1(a). The former two denote lattice and plastic deformations; the latter two represent micro-homogeneous and micro-heterogeneous deformations, respectively.

3. ATOMIC HOMOGENIZATION

3.1 Basic Considerations

The equations thus far have referred to continuum conservation. To introduce the notion of discrete atoms, define spatial positions $z_{\langle j \rangle}^{a}$ of atoms in configuration B in Cartesian coordinates:

$$z_{\langle j \rangle}^{a} = \delta_{.\alpha}^{a} \tilde{Z}_{\langle j \rangle}^{\alpha} + q_{\langle j \rangle}^{a}, \qquad (7)$$

with $\mathbf{q}_{\langle j \rangle}$ a displacement vector between intermediate and current states. Let $\tilde{\mathbf{R}}_{\langle j \backslash k \rangle}$ and $\mathbf{r}_{\langle j \backslash k \rangle}$ denote interatom vectors in respective configurations $\tilde{B}$ and B, i.e.,

$$\tilde{\mathbf{R}}_{\langle j \backslash k \rangle} = \tilde{\mathbf{Z}}_{\langle k \rangle} - \tilde{\mathbf{Z}}_{\langle j \rangle}, \qquad \mathbf{r}_{\langle j \backslash k \rangle} = \mathbf{z}_{\langle k \rangle} - \mathbf{z}_{\langle j \rangle}. \qquad (8)$$

Making contact with the homogenization theory of Section 2, we define

$$z_{\langle j \rangle}^{a} = \overline{F}_{\langle jk \rangle \alpha}^{L\,a} \tilde{Z}_{\langle k \rangle}^{\alpha} + \tilde{v}_{\langle j \rangle}^{a}. \qquad (9)$$

The first term in Eq. (9), $\overline{F}_{\langle jk \rangle \alpha}^{L\,a} \tilde{Z}_{\langle k \rangle}^{\alpha}$, accounts for the uniform projection over each periodic cell of the macroscopic lattice deformation field to the fine scale (i.e., the Cauchy-Born approximation), and $\tilde{v}_{\langle j \rangle}^{a}$ is the discrete atomistic analog of the perturbation in displacement due to microscopic heterogeneity.

The mapping $\mathbf{F}^{\mathbf{P}}$ represents the cumulative deformation of the material, but not the lattice, due to dislocation glide through the unit cell. For a fixed control volume, once atoms have convected through the lattice due to $\mathbf{F}^{\mathbf{P}}$, B_0 and $\tilde{B}$ appear identical in the fine scale domain if no dislocations are created or destroyed within the volume element, yet net deformation of the material will have taken place at the coarse scale (Asaro, 1983). For a purely plastic process with $\mathbf{F}^{\mathbf{L}} = \mathbf{1}$, new atoms would enter the control volume (i.e., the atomic unit cell) in the identical locations as the old, to replace those that exited due to plastic flow. The concept is illustrated in Fig. 1(b).

3.2 Elastoplastic Atomistic Homogenization

We assume a free energy potential depending only upon the relative positions of all atoms (i.e., lattice statics) $\tilde{\Psi} = \tilde{\Psi}\left(\mathbf{q}_{\langle j \rangle}, \tilde{\mathbf{Z}}_{\langle j \rangle} \right) = \tilde{\Psi}\left(\mathbf{r}_{\langle 1 \backslash 2 \rangle}, \mathbf{r}_{\langle 1 \backslash 3 \rangle}, \mathbf{r}_{\langle 2 \backslash 3 \rangle}, \dots \mathbf{r}_{\langle \mathbb{N}-1 \backslash \mathbb{N} \rangle} \right)$. Under isothermal conditions, we may rewrite this as

$$\tilde{\Psi} = \tilde{\Psi}\left(\mathbf{F}^{\mathbf{L}}, \tilde{\xi} \right), \qquad (10)$$

where $\tilde{\xi}$ accounts for effects on stored energy due to deviations from homogeneous elasticity at the fine scale.
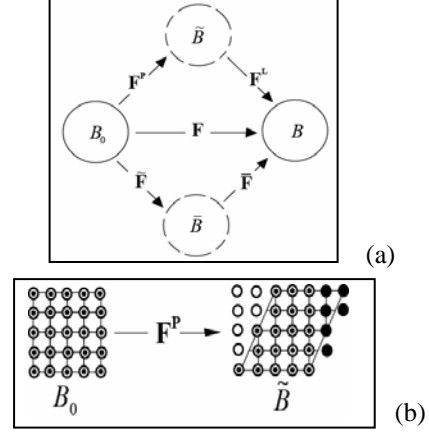

(a)

(b)

Figure 1. Deformation mappings and configurations (a), and purely plastic deformation (b).

After considerable equation derivation, we arrive at the analogous atomistic set of homogenization equations

$$\mathcal{D}_{\langle j \rangle ab}^{\beta}\left(\frac{\partial \overline{u}^{b}}{\partial X^{A}} + \delta_{.A}^{b} - \delta_{.\chi}^{b} F_{.A}^{P\chi} \right) F_{.\beta}^{P-1A} = \mathcal{H}_{\langle jk \rangle ab} \tilde{v}_{\langle k \rangle}^{b}, \qquad (11)$$

$$\frac{1}{Y} \int_{Y} \int_{V} \overline{\mathbb{C}}_{ba}^{AB}\left(\frac{\partial \overline{u}^{b}}{\partial X^{A}} + \delta_{.A}^{b} - \delta_{.\chi}^{b} F_{.A}^{P\chi} \right) \frac{\partial(\delta \overline{u}^{a})}{\partial X^{B}} dVdY =$$

$$\int_{\partial V} T^{a} g_{ab} \delta \overline{u}^{b} dA + \int_{V} B^{a} g_{ab} \delta \overline{u}^{b} dV + \qquad (12)$$

$$\frac{1}{Y} \int_{Y} \int_{V} \overline{\mathcal{D}}_{\langle j \rangle ba}^{B} \tilde{v}_{\langle j \rangle}^{b} \frac{\partial(\delta \overline{u}^{a})}{\partial X^{B}} dVdY.$$

where $\mathcal{D}_{\langle j \rangle ab}^{\beta} = -\partial^{2}\tilde{\Psi}/\partial q_{\langle j \rangle}^{a} \partial F_{.\beta}^{Lb}$, $\mathcal{H}_{\langle k \rangle ab} = \partial^{2}\tilde{\Psi}/\partial q_{\langle k \rangle}^{a} \partial q_{\langle j \rangle}^{b}$, $\overline{\mathbb{C}}_{ba}^{AB} = J^{P-1} F_{.\alpha}^{P-1B} \hat{\mathbb{C}}_{ba}^{\beta\alpha} F_{.\beta}^{P-1A}$ and $\overline{\mathcal{D}}_{\langle j \rangle ba}^{B} = J^{P-1} F_{.\alpha}^{P-1B} \mathcal{D}_{\langle j \rangle ba}^{\alpha}$. In subsequent calculations, (11) is solved for the (atomic) inner displacements $\tilde{v}_{\langle k \rangle}^{b}$ and (12) can be solved using a standard numerical procedure such as a finite element method.

3.3 Inelastic fields and defect kinetics

For simplicity, temperatures are presently omitted. Therefore, additional kinetic equations are required to advance the plastic deformation gradient $\mathbf{F}^{\mathbf{P}}$ and internal variables $\tilde{\xi}$. In the continuum description, these are written as

$$\dot{\mathbf{F}}^{\mathbf{P}} = \dot{\mathbf{F}}^{\mathbf{P}}\left(\mathbf{F}, \mathbf{F}^{\mathbf{P}}, \tilde{\xi}, \theta \right), \qquad (13)$$

$$\dot{\tilde{\xi}} = \dot{\tilde{\xi}}\left(\mathbf{F}, \mathbf{F}^{\mathbf{P}}, \tilde{\xi}, \theta \right). \qquad (14)$$

One can formulate an approximate expression for the rate of the mapping $\dot{\mathbf{F}}^{\mathbf{P}}$ in terms of the dislocation velocity, line length, and orientation (Teodosiu, 1969).

A similar approach has been used by Zbib and co-workers in the context of discrete dislocation plasticity (Zbib & de la Rubia, 2002). The determination of $\dot{\mathbf{F}}^P$ is nontrivial. In the absence of temperatures, we must assume specific forms in section 4.3.

3.4. Numerical Implementation

In cases of monotonically loaded crystals, we employ the improved computer procedure of (Clayton & Chung, 2006) wherein a full solution to Eq. (11) is evaluated only for the first load step and subsequent steps are obtained via the minimization of a scalar numerical parameter η^i, through a line search algorithm. This is achieved by a modification to (9) such that it now reads

$$z^{a\ i}_{\langle j \rangle} = \overline{F}^{L\,a\ i}_{\langle jk \rangle \alpha} \tilde{Z}^{\alpha}_{\langle k \rangle} + \tilde{\tilde{v}}^{a\ i}_{\langle j \rangle} \qquad (15)$$

where the index i is the load increment and $\tilde{\tilde{v}}^{a\ i}_{\langle j \rangle}$ is defined by $\tilde{\tilde{v}}^{a\ i}_{\langle j \rangle} = \eta^i \tilde{v}^a_{\langle j \rangle}$.

4. APPLICATION: DEFECTS IN TUNGSTEN

The present formulation is applied to study the mechanical behavior of tungsten (W), a BCC transition metal of relatively high mass density. Its combination of high density and strength make it an attractive material for use in defense applications such as ordnance (Zhou & Clifton, 1997; Clayton, 2005). Specifically computed here are the nonlinear elastic responses of deforming W crystals containing (i) vacancies, (ii) screw dislocations of like sign and screw dislocation dipoles, or (iii) low-angle twist boundaries. In section 4.2, unit cells are deformed in uniaxial stretch to 2.5% elongation or larger. The computational method is demonstrated by direct comparison with conjugate gradient-based lattice statics. This is followed by results in section 4.3 of larger-deformation shear simulations (to 10% applied shear strain) reported for the case of screw dislocation glide in BCC W, in which the evolving intermediate configuration is updated assuming monotonic single slip occurs as resolved shear stresses exceed the Peierls threshold (cf. Hirth & Lothe, 1982).

4.1 Atomistic potential: tungsten

Without loss of generality in the underlying method, we employ an empirical $\mathbb{N}$-body potential specifically developed for transition metals (Finnis & Sinclair, 1984) in order to estimate the free energy potential $\tilde{\Psi}$ of (10). Duesberry & Vitek (1998) exercised the Finnis-Sinclair potential to model screw dislocation core structures, construct generalized stacking fault energy surfaces, and predict plastic slip anisotropy (i.e. tension-compression

asymmetry in the yield function) in multiple BCC transition metals.

4.2 Static defects in tungsten

The calculations are performed to determine the effective tangent stiffness of a microscopic (i.e., atomistic) unit cell. A sample atomistic unit cell representative of all calculations described in the present work is shown in Fig. 2. The unit cell dimensions are $L_1 \times L_2 \times L_3 = a\sqrt{3}N_1 \times a\sqrt{6}N_2 \times a\sqrt{2}N_3$, where N_1, N_2, and N_3 are respectively the number of repeating planes stacked in the [111]-, [11$\overline{2}$]-, and [1$\overline{1}$0]- directions. Periodic boundaries in the form of wrap-around conditions are applied along all faces of the unit cell in the usual manner (cf. Vitek, 1976).
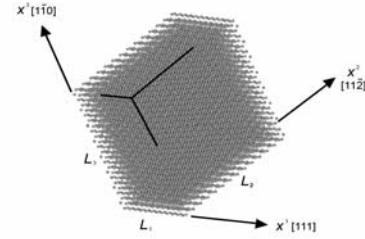

Figure 2. Atomistic scale unit cell for perfect BCC lattice.

First, we examine the response of W containing unit cells with immobile but deformable lattice defects, i.e. the local deformation gradient $\mathbf{F} = \mathbf{F}^L = \overline{\mathbf{F}}\tilde{\mathbf{F}}$ in the context of Fig. 1. Fundamental material effects in the context of lattice statics calculations have been examined by (Vitek, 1976; Duesberry & Vitek, 1998).

The initial atomic coordinates are found using a two-step procedure: first the linear-elastic solution for displacement field of the defect is applied to the atoms, then a conjugate gradient algorithm (Plimpton & Hendrickson, 1993) is used to find local minimum energy atomic positions. The homogenization method then proceeds to find the changes in local states with applied deformation. The applied (i.e., coarse-scale) deformation gradient field (in conjunction with fine-scale periodicity) is uniaxial stretching in the [111]-direction over a range of $1.000 \le F_{11} \le 1.025$. We verify the computed configurations by comparing to incremental conjugate gradient (CG) energy minimization used in conventional lattice statics.

4.2.1 Point Vacancy

The initial configuration for the point vacancy is constructed by removing one atom closest to the centroid of the unit cell. The defect density in this case is defined as the volume fraction of missing atoms, i.e., $\rho^d = 1/\mathbb{N}$,
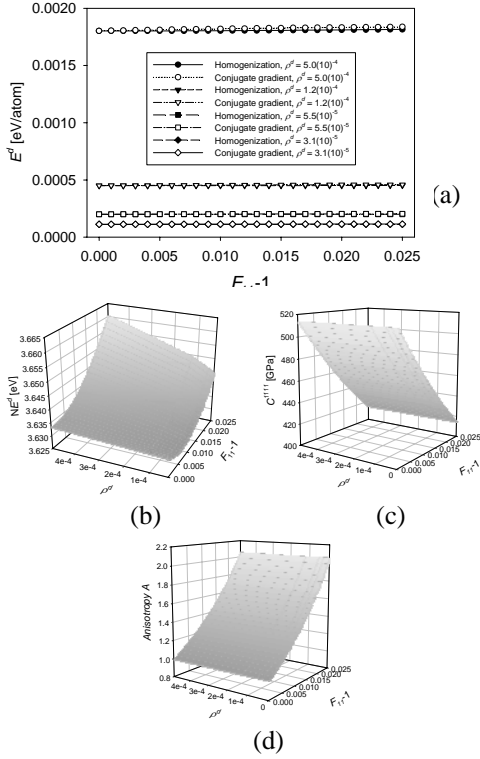
Figure 3. Vacancy configuration: (a) strain energy comparison between computational methods, (b) defect energy, (c) elastic stiffness, and (d) Zener anisotropy.

where $\mathbb{N}$ is the total number of atoms prior to vacancy creation ranging from 2016 to 32256. Fig. 3(a) shows the defect energy comparison with CG. The agreement is excellent. In Fig. 3(b-d) are, respectively, the defect energy under variations of the defect density, the elastic stiffness C^{1111}, and the Zener anisotropy factor A, all under parametric variations of the defect density. The Zener anisotropy factor A is defined by (cf. Hirth & Lothe, 1982)

$$ A = \frac{2C^{1212}}{C^{1111} - C^{1122}} = \frac{2\hat{\mathbb{C}}_{11}^{22}}{\hat{\mathbb{C}}_{11}^{11} - \hat{\mathbb{C}}_{11}^{12}} . \tag{16} $$

Note that defect-free W is nominally isotropic at null deformation, i.e., $A = 1.00$, and that the anisotropy increases dramatically as the lattice is stretched. First-principles (i.e., quantum-mechanical) calculations have indicated a departure from isotropy in W at large pressures (Ruoff et al., 1998).

4.2.2 Screw Dislocation

The dislocation tangent line and burgers vector **b** for the screw dislocation example are oriented along the [111]-direction and pass through the centroid of the unit cell, the latter having a magnitude of $b = |\mathbf{b}| = \sqrt{3}a/2$. The scalar dislocation density is defined as the defect line length per unit reference volume, i.e., $\rho^d = 1/(L_2 L_3)$. The defect energy per atom, as shown in Fig. 4(a), is computed accurately by our homogenization scheme as verified by the incremental CG solutions. We see a linear increase in stored defect energy with F_{11}, and a roughly linear increase with increasing ρ^d. Gibeling & Nix (1980) discussed, from the standpoint of discrete dislocation modeling, how the strain energy supported by dislocations may be amplified by applied external deformations, and Clayton (2005) assumed a linear dependence of stored elastic energy on dislocation density in a continuum crystal plasticity model of single crystalline W. From Fig. 4(c) and Fig. 4(d), the dislocation density tends to accelerate the decrement in C^{1111} with increasing applied stretch, whereas A tends to be suppressed by increasing dislocation content as the stretch increases. Although the trend of decreasing elastic modulus with dislocation content has been reported from physical experiments (Smith, 1953) and analytical continuum modeling (Lebedev, 1996), it has not been emphasized previously in continuum plasticity models.

4.2.3 Screw Dislocation Dipole

The dislocation tangent lines for the screw dislocation dipole are oriented along the [111]-direction. The pair with opposite burgers vector signs are located at $(\tfrac{1}{4}L_2, \tfrac{1}{4}L_3)$ and $(\tfrac{3}{4}L_2, \tfrac{3}{4}L_3)$, maintaining a minimum separation distance of $(\tfrac{1}{2}L_2, \tfrac{1}{2}L_3)$ between all dislocations whether within the cell or in images.

The dislocation density $\rho^d = 2/(L_2 L_3)$, and the net Nye (1953) tensor vanishes, as the burgers vectors cancel out, meaning the dislocation density is 'statistically stored' in the sense of Ashby (1970). The defect energy computed with our homogenization scheme is plotted in Fig. 5(a); again, in good agreement with CG simulations. From Fig. 5(b), we see that E^d increases linearly with ρ^d, and it increases linearly with F_{11}. As shown in Fig. 5(c), the stiffness coefficient C^{1111} decreases with increasing defect density and increasing stretch. Anisotropy A (Fig. 5(d)) increases with stretch and increases with dislocation content at low values of ρ^d ($\leq 0.013/\text{nm}^2$), but decreases as ρ^d is increased further.

4.2.4 Low Angle Twist Grain Boundary

The final defect configuration examined is a low angle twist grain boundary. We describe this boundary type using the disclination concept (Li, 1972; Clayton et
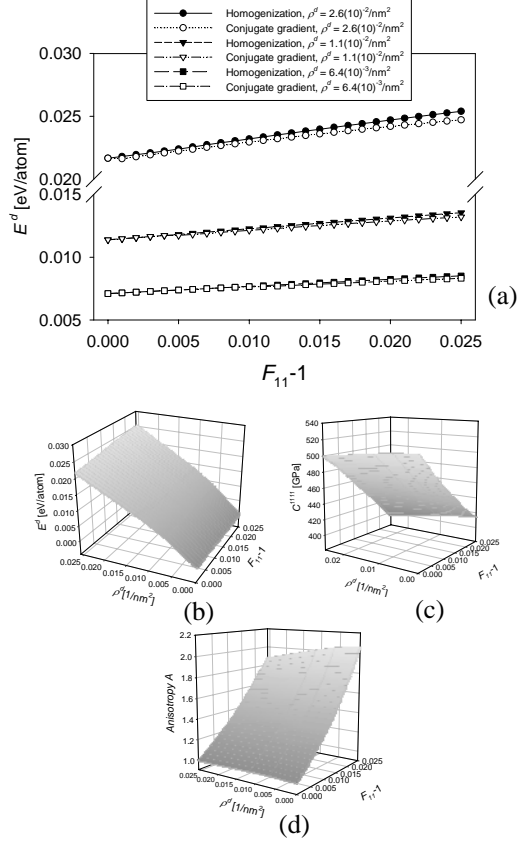
Figure 4. Screw dislocation: (a) strain energy comparison between computational methods, (b) defect energy, (c) elastic stiffness, and (d) Zener anisotropy (e).

al., 2006). The defect misorientation across the (110)-plane is $\omega = 0.2 \text{ radians}$, a value that ensures a stable local configuration for the initial atomic arrangement. The Frank vector is oriented parallel to $[1\overline{1}0]$, the disclination line $\boldsymbol{i}$ is oriented along $[111]$, and the axis of twist passes through the cell centroid. The disclination line density is $\rho^d = 1/(L_2 L_3)$. The defect energy results under deformation are again validated via comparison with an incremental conjugate gradient solution in Fig. 6(a). The agreement is once again very good. From Fig. 6(b), E^d increases nonlinearly with disclination line density; that is, it increases nonlinearly with grain boundary area per unit volume.

Note that we are essentially simulating a periodic array of such low-angle grain boundaries, as have been known to appear in pure W subjected to severe plastic deformation (Valiev et al., 2002; Wei et al., 2005). In contrast to the other classes of defects examined in the present work, the defect energy decreases with applied stretch, and the stiffness component C^{1111} increases with increasing defect density. From Fig. 6(c), at null applied strain, C^{1111} increases from 514 GPa to 520 GPa as the

defect density ρ^d is increased from 0 to 0.026/nm². At an applied stretch of $F_{11} = 1.025$, C^{1111} increases over the same range of ρ^d from 414 GPa to 419 GPa. Anisotropy, shown in Fig. 6(d), is suppressed slightly with increasing disclination content.

4.3 Multiscale elastoplasticity

Since the flux of dislocations leaves the crystal lattice relatively unperturbed upon complete glide across the periodic unit cell, we appeal to the notion of an evolving relaxed intermediate or natural configuration (Bilby et al., 1957; Teodosiu, 1969; Asaro, 1983) and introduce it explicitly into the formulation in this paper for plasticity. In the approach, finite inelastic deformation is accounted for by the evolution of this relaxed configuration, as dictated by the dislocation flux through the volume element. The instantaneous thermoelastic response of the element is measured with respect to the natural configuration, and driving forces for defect propagation are calculated at the current state or time instant, in order to project the intermediate configuration forward temporally.

The full decomposition $\mathbf{F} = \mathbf{F}^L \mathbf{F}^P = \overline{\mathbf{F}} \tilde{\mathbf{F}}$ of Fig. 2 applies. Initial conditions for the unit cell are identical to those of Fig. 4(a). We apply pure shear deformation in the 1-3 plane, over the range $0.00 \le F_{13} \le 0.10$. The multiplicative decomposition $\mathbf{F} = \mathbf{F}^L \mathbf{F}^P$ yields

$$F_{13} = \gamma = \gamma^L + \gamma^P, \tag{17}$$

where γ^L is the lattice shear associated with the external stress and γ^P is the cumulative plastic slip, assumed in our idealized problem here to occur as a result of dislocation glide on (110)- planes. Plastic slip is assumed to follow the simple kinetic relation

$$\gamma^P = \gamma - \gamma_0^y - \frac{\gamma_1^y}{2}\left\{1 + \sin\left[\begin{matrix}(2\pi/\alpha b) \times \\ (\gamma - \gamma_0^y - \alpha b/4)\end{matrix}\right]\right\}, \tag{18}$$

for $(\forall \gamma \ge \gamma_0^y)$, and $\gamma^P = 0$ otherwise, where γ_0^y is the initial yield strain, γ_1^y is an additional lattice strain required to overcome the Peierls barrier, and $\alpha = 1/L_3$ scales the amount of shear strain accumulated in the unit cell due to the slip of a dislocation over the distance of one burgers vector. The sinusoidal character of (20) is in accordance with the Peierls model of periodic lattice resistance stress discussed by Hirth & Lothe (1982). The simulations discussed here assume that the primary dislocation remains fixed in the unit cell (in the atomistic domain), and that no defect generation or annihilation

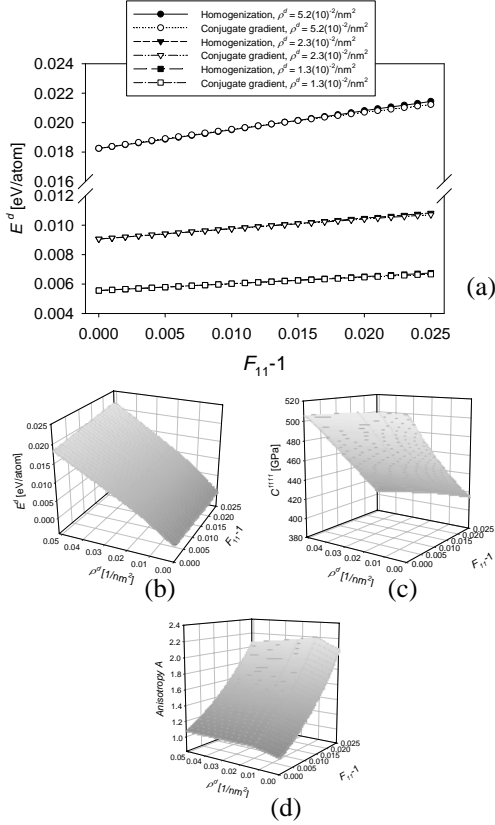occurs, as other screw dislocations convect through the lattice and cause an increase in plastic shear γ^P.

(a)

(b)

(c)

(d)

Figure 5. Screw dislocation dipole: (a) strain energy comparison between computational methods, (b) defect energy, (c) elastic stiffness, and (d) Zener anisotropy.

Following the molecular statics calculations of Vitek (1976), we choose $\gamma_0^y = 0.020$ and $\gamma_1^y = 0.009$, the former a shear strain required to cause $[111](1\overline{1}0)$ - screw dislocation core shuffling in BCC W, the latter following his result that a total shear strain of 0.029 is required to sustain steady dislocation glide.

The 1-3 shear component of the first Piola-Kirchhoff stress, P^{13}, is shown in Fig. 7(a), where components of the stress tensor **P** are computed from

$$P_a^{.A} = J^{P-1} \frac{\partial \tilde{\Psi}}{\partial F_{.\alpha}^{La.}} F_{.\alpha}^{P-1A}. \tag{19}$$

Prior to initial yield, slight differences in slope of the stress-strain response are evident among the three curves, each curve corresponding to a different dislocation density ρ^d. Such differences are due in part to the decrease in effective elastic shear modulus, $C^{1313} = \hat{\mathbb{C}}_{33}^{11}$, with increasing defect density, as is seen in Fig. 7(b).

Upon initial yield, the stress-strain curves follow Peierls-type oscillations (a consequence of using (18)), with each period corresponding to the passage of a single [111]-screw dislocation across the unit cell, gliding on a (110)-plane. As the dislocation density ρ^d is inversely related to the dimension L_3 of the unit cell, the larger the dislocation density, the smaller the unit cell size, the larger increment in shear strain γ^P associated with the passage of each dislocation, and the longer the period of shear stress oscillations in Fig. 7(a). In the absence of such oscillations, the material behavior would be elastic-perfectly-plastic. The total energy per atom, $E^t = \tilde{E}/\mathbb{N} - U^c$, is shown in Fig. 7(c). At zero applied shear, differences among energy curves are due purely to differences in defect concentration, while the energy oscillations at larger shear deformations, $F_{13} > 0.020$, are associated with the lattice deformation fields ($\mathbf{F^L}$) appearing in conjunction with the applied stress.

5. DISCUSSION & CONCLUSIONS

A multiscale method predicated on asymptotic homogenization has been developed and implemented. The technique is based on conservation principles formulated using deformation gradients at both micro and macro scales. Aside from self-periodicity near the boundaries, no restriction is placed on the atomic structure or for continuity with the supporting continuum. Thus the formulation directly accounts for the effects of lattice defects on the homogenized mechanical properties, as well as the lattice-preserving kinematics of finite plastic deformation associated with dislocation flux, all as functions of the state of deformation. From a computational standpoint, the homogenization method has been demonstrated to accurately reproduce lattice statics in terms of prediction of minimum energy in statically-deforming lattices containing defects. It enables the consideration of very large continuum scales with finite nontrivial atomic structures embedded within.

The homogenization method was implemented numerically to study the nonlinear elastic response of BCC tungsten lattices containing periodically-distributed vacancies, screw dislocations and dipoles, and low-angle twist boundaries. The material results showed that general trends of defect structures subject to strain are in agreement with past observations and with strong quantitative agreement with computed fundamental material properties. Both static and initial dynamics results show conclusive agreement with alternative, more costly approaches.
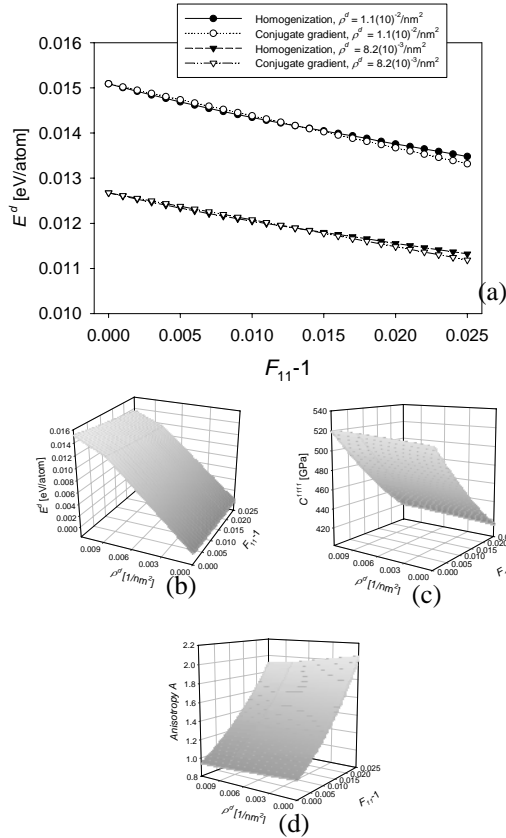
Figure 6. Twist disclination: (a) strain energy comparison between computational methods, (b) defect energy, (c) elastic stiffness, and (d) Zener anisotropy.

REFERENCES

Asaro, R.J., 1983. Crystal plasticity. J. Appl. Mech. 50, 921-934.

Ashby, M.F., 1970. Phil. Mag. 21, 399-424.

Bilby, B.A., Gardner, L.R.T., and Stroh, A.N., 1957. In: Proc. 9th Int. Congr. Appl. Mech. Bruxelles, Vol. 8, Univ. Bruxelles, pp. 35-44.

Chung, P.W., 2004. Int. J. Numer. Meth. Eng. 60, 833-859.

Chung, P.W. and Namburu, R.R., 2003. Int. J. Solids Structures 40, 2563-2588.

Clayton, J.D., 2005. J. Mech. Phys. Solids 53, 261-301.

Clayton, J.D., McDowell, D.L., and Bammann, D.J., 2006. Int. J. Plasticity 22, 210-256.

Clayton, J. D., Chung, P. W., 2006. J. Mech. Phys. Solids, 54, 1604.

Cole, M. W., W.D. Nothwang, C. Hubbard, E. Ngo, and M. Ervin, J. Appl. Phys. 93, 9218, 2003.

Duesberry, M.S. and Vitek, V., 1998. Acta Mater. 46, 1481-1492.

Dupuy, L.M., Tadmor, E.B., Miller, R.E., and Phillips, R., 2005. Phys. Rev. Letters 060202.

Ericksen, J.L., 1984. Phase Transformations and Material Instabilities in Solids. Academic Press Inc., pp. 61-77.

Finnis, M.W. and Sinclair, J.E., 1984. Phil. Mag. A 50, 45-55.

Ghoniem, N.M., Busso, E.P., Kioussis, N., and Huang, H., 2003. Phil. Mag. 83, 3475-3528.

Gibeling, J.C. and Nix, W.D., 1980. Acta Metall. 28, 1743-1752.

Hirth, J.P. and Lothe, J., 1982. Theory of Dislocations. Second Edition, Krieger, Malabar, FL.

Lebedev, A.B., 1996. Phil. Mag. A 74, 137-150.

Li, J.C.M., 1972. Surf. Sci. 31, 12-26.

Nye, J.F., 1953 Acta Metall. 1, 153-162.

Plimpton, S.J. and Hendrickson, B.A., 1993. MRS Proceedings 291, Pittsburgh, PA, p. 37.

Rudd, R.E. and Broughton, J.Q., 2000. Phys. Stat. Sol. B 217, 251-291.

Ruoff, A.L., Rodriguez, C.O., and Christensen, N.E., 1998. Phys. Rev. B 58, 2998-3002.

Seppälä, E.T., Belak, J., and Rudd, R.E., 2004. Phys. Rev. B 69, 134101.

Smith, A.D.N., 1953. Phil. Mag. A 44, 453-466.

Tadmor, E.B., Ortiz, M., and Phillips, R., 1996. Phil. Mag. A 73, 1529-1563.

Teodosiu, C., 1969. In: Fundamental Aspects of Dislocation Theory. NBS Special Publication 317, U.S. Government Printing Office, Gaithersburg, MD, pp. 837-876.

Valiev, R.Z., Islamgaliev, R.K., Tumentsev, A.N., 2002. Solid State Phenomena 87, 255-264.

Vitek, V., 1976. Proc. R. Soc. Lond. A 352, 109-124.

Wei, Q., Ramesh, K.T., Ma, E., Kecskes, L.J., Dowding, R.J., Kazykhanov, V.U., and Valiev, R.Z., 2005. Applied Physics Letters 86, 101907.

Zbib, H.M., and de la Rubia, T.D., 2002. Int. J. Plasticity 18, 1133-1163.

Zhou, M. and Clifton, R.J., 1997. J. Applied Mech. 64, 487-494.
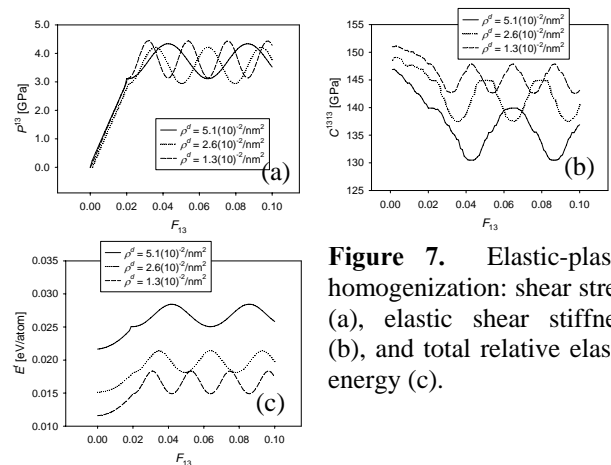
Figure 7. Elastic-plastic homogenization: shear stress (a), elastic shear stiffness (b), and total relative elastic energy (c).

A Multiscale Modeling Method for Deformations on Atomic Lattice Defects and Application to Plasticity

Peter W. Chung

Computational and Engineering Sciences Branch

Army Research Laboratory, MD, USA

John D. Clayton

Impact Physics Branch

Army Research Laboratory, MD, USA

25th Army Science Conference
November 27-30, 2006

25th **ARMY SCIENCE CONFERENCE**
Transformational Army Science & Technology - Charting the future of S&T for the Soldier

Overview

1. Background: crystal kinematics

2. Homogenization

   - Length scales and coordinate systems

   - Elastic continua

   - Elastic – plastic continua

   - Atoms – discreteness at the fine scale

3. Defects in Body-Centered-Cubic tungsten

   - Atomistic potential

   - Numerical results: vacancy, dislocation, twist boundary

   - Numerical results: screw dislocation with continuum plasticity

Deformation kinematics of crystalline solids

Perfect lattice [Cauchy, 1828; Born, 1914; Ericksen, 1984; Zanzotto, 1992]
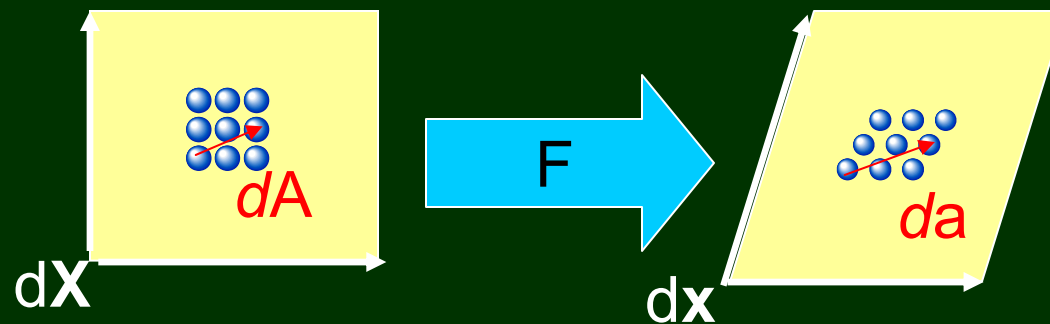
Continuum mechanics: $d\mathbf{x}=\mathbf{F}d\mathbf{X}$
Born-rule mechanics: $d\mathbf{a}=\mathbf{F}d\mathbf{A}$

Imperfect lattice: Born rule does not apply

$d\mathbf{x}=\mathbf{F}d\mathbf{X}$ **but** $d\mathbf{a} \neq \mathbf{F}d\mathbf{A}$
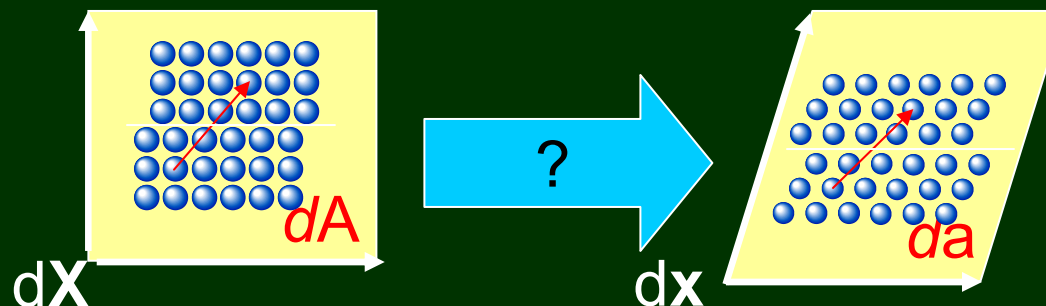
Multiscale scheme: coordinates and configurations

Externally unstrained configuration
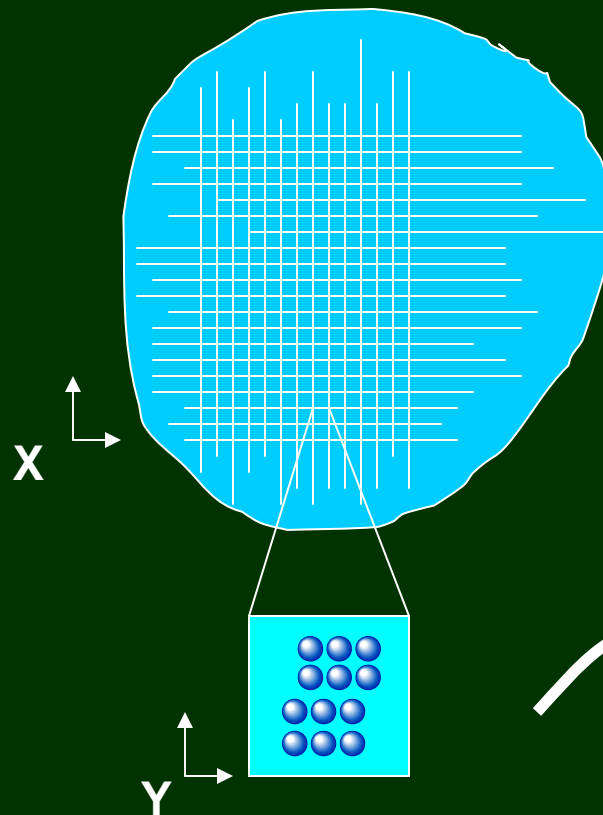
Deformed configuration

X

x

Y

y
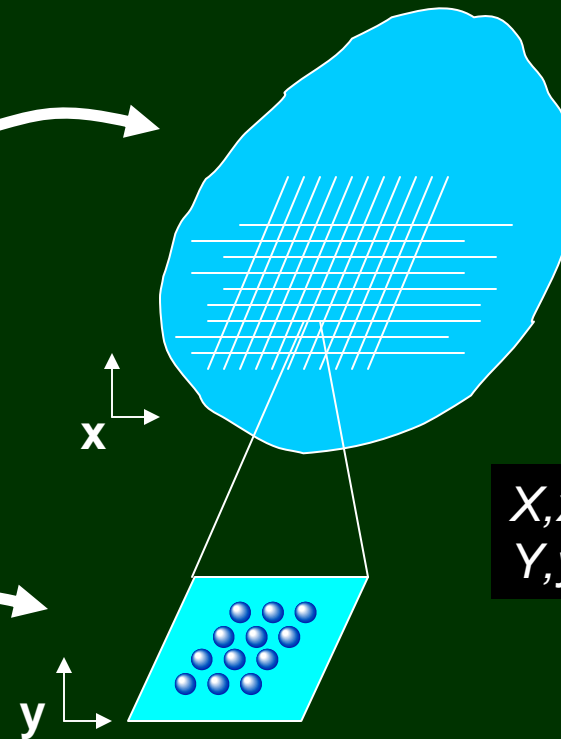
X,x: coarse scale
Y,y: fine scale

[Bensoussan et al., 1978; Sanchez-Palencia, 1980; Bakhvalov & Panasenko, 1989; Chung & Namburu, 2003; Chung, 2004]

Asymptotic homogenization with geometrically-nonlinear elasticity

Kinematics (displacements)

$$x^a = \varepsilon y^a$$

$$X^A = \varepsilon Y^A$$

(ε is a small scalar)

$$u^a = \bar{u}^a + \varepsilon \tilde{v}^a + \varepsilon^2 \tilde{w}^a + ...$$

$(x, X, u: \text{ coarse scale})$
$(y, Y, v: \text{ fine scale, periodic})$

Virtual work principle (statics)

$$\int_V P^{aB} g_{ab} \left(\delta u\right)^b_{\,|B} dV = \int_{\partial V} T^a g_{ab} \delta u^b dA + \int_V B^a g_{ab} \delta u^b dV$$

Hyperelasticity

$$\Psi = \Psi(\mathbf{F})$$

$$\mathbf{F} = \frac{\partial \mathbf{x}}{\partial \mathbf{X}}$$

$$\mathbf{P} = \frac{\partial \Psi}{\partial \mathbf{F}}$$

Substituting, integrating over *Y*, and lim $\varepsilon \to 0$ gives

$$\frac{1}{Y} \int_Y \int_V \frac{\partial \Psi}{\partial F^a_{.B}} \frac{\partial (\delta \tilde{v}^a)}{\partial Y^B} dV dY = 0 \quad \left(\forall \delta \tilde{v}^a\right)$$

coupled micro- and macro- equations; solve concurrently for $\tilde{v}^a$ and $\bar{u}^a$

$$\frac{1}{Y} \int_Y \int_V \frac{\partial \Psi}{\partial F^a_{.B}} \frac{\partial (\delta \bar{u}^a)}{\partial X^B} dV dY = \int_{\partial V} T^a g_{ab} \delta \bar{u}^b dA + \int_V B^a g_{ab} \delta \bar{u}^b dV \quad \left(\forall \delta \bar{u}^a\right)$$

Kinematics (displacements)

$$u^a = \overline{u}^a + \tilde{u}^a = \overline{u}^a + \varepsilon \tilde{v}^a$$

$$x^a = \varepsilon y^a \qquad X^A = \varepsilon Y^A$$

Hyperelasticity with defects

$$\tilde{\Psi} = \tilde{\Psi}(\mathbf{F^L}, \tilde{\boldsymbol{\xi}}) \qquad \tilde{\Psi} = J^{P-1}\Psi$$

$$\tilde{S}^{\alpha\beta} = g^{ab}\frac{\partial \tilde{\Psi}}{\partial F^{Lb}_{.\alpha}}F^{L-1\beta}_{.a} = 2\frac{\partial \tilde{\Psi}}{\partial \tilde{C}_{\alpha\beta}} = \frac{\partial \tilde{\Psi}}{\partial \tilde{E}_{\alpha\beta}}$$

Deformation gradient

$$\mathbf{F} = \mathbf{F^L}\mathbf{F^P}$$

$\mathbf{F^P}$ is lattice-preserving
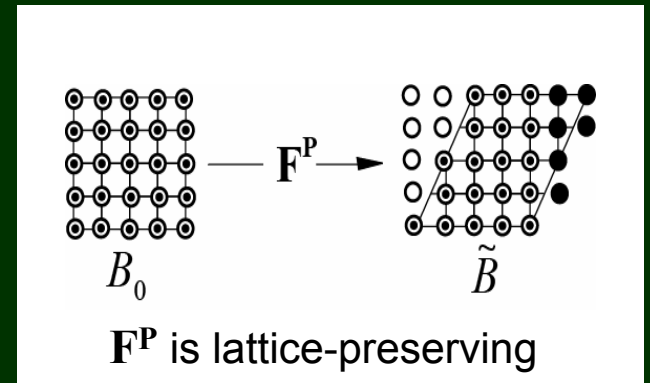
Fine and coarse scale equilibrium from virtual work principle

$$\lim \varepsilon \to 0 :$$

$$\frac{1}{Y}\int_Y\int_V J^{P-1}F^{P-1B}_{.\alpha}\frac{\partial \tilde{\Psi}}{\partial F^{La}_{.\alpha}}\frac{\partial(\delta \tilde{v}^a)}{\partial Y^B}\,dV\,dY = 0 \qquad \left(\forall \delta \tilde{v}^a\right)$$

$$\frac{1}{Y}\int_Y\int_V J^{P-1}F^{P-1B}_{.\alpha}\frac{\partial \tilde{\Psi}}{\partial F^{La}_{.\alpha}}\frac{\partial(\delta \overline{u}^a)}{\partial X^B}\,dV\,dY = \int_{\partial V}T^a g_{ab}\delta\overline{u}^b\,dA + \int_V B^a g_{ab}\delta\overline{u}^b\,dV \qquad \left(\forall \delta \overline{u}^a\right)$$

Incorporation of atomic kinematics at fine scale

Discrete kinematics (Cartesian space)

$$z^a_{\langle m\rangle} = \delta^a_\alpha \tilde{Z}^\alpha_{\langle m\rangle} + q^a_{\langle m\rangle}$$

atom displacements

$$\tilde{\mathbf{R}}_{\langle a\backslash b\rangle} = \tilde{\mathbf{Z}}_{\langle b\rangle} - \tilde{\mathbf{Z}}_{\langle a\rangle}$$

$$\mathbf{r}_{\langle a\backslash b\rangle} = \mathbf{z}_{\langle b\rangle} - \mathbf{z}_{\langle a\rangle}$$

relative atom positions

$$\overline{F}^{La}_{\langle mn\rangle\alpha} = F^{La}_{.\alpha}\delta_{\langle mn\rangle}$$

$$z^a_{\langle m\rangle} = \overline{F}^{La}_{\langle mn\rangle\alpha}\tilde{Z}^\alpha_{\langle n\rangle} + \tilde{v}^a_{\langle m\rangle}$$

lattice mapping

defect perturbation

$$\mathbf{r}_{\langle a\backslash b\rangle} = \overline{\mathbf{F}}^{\mathbf{L}}\tilde{\mathbf{R}}_{\langle a\backslash b\rangle} + \tilde{\mathbf{v}}_{\langle b\rangle} - \tilde{\mathbf{v}}_{\langle a\rangle} = \overline{\mathbf{F}}^{\mathbf{L}}\tilde{\mathbf{R}}_{\langle a\backslash b\rangle} + \tilde{\mathbf{r}}_{\langle a\backslash b\rangle}$$

Cauchy-Born rule

correction

Molecular statics approximation (0 K)

$$\tilde{\Psi} = \tilde{\Psi}\left(\mathbf{q}_{\langle m\rangle}, \tilde{\mathbf{Z}}_{\langle m\rangle}\right) = \tilde{\Psi}\left(\mathbf{r}_{\langle 1\backslash 2\rangle}, \mathbf{r}_{\langle 1\backslash 3\rangle}, \mathbf{r}_{\langle 2\backslash 3\rangle}, \ldots \mathbf{r}_{\langle \square -1\backslash \square\rangle}\right)$$

$$\tilde{\Psi} = \tilde{\Psi}\left(\mathbf{F}^{\mathbf{L}}, \tilde{\xi}\right)$$

Fine scale equilibrium (after some algebra)

$$\mathcal{D}^\beta_{\langle j\rangle ab}\frac{\partial \overline{u}^b}{\partial X^A}F^{P-1A}_{.\beta} = \mathcal{H}_{\langle jk\rangle ab}\tilde{v}^b_{\langle k\rangle}$$

Coarse scale equilibrium

$$\frac{1}{Y}\int_Y\int_V \overline{\square}^{AB}_{ba}\left(\frac{\partial \overline{u}^b}{\partial X^A} + \delta^b_{.A}\right)\frac{\partial(\delta\overline{u}^a)}{\partial X^B}dVdY =$$

$$\int_{\partial V}T^a g_{ab}\delta\overline{u}^b dA + \int_V B^a g_{ab}\delta\overline{u}^b dV + \frac{1}{Y}\int_Y\int_V \overline{\mathcal{D}}^B_{\langle j\rangle ba}\tilde{v}^b_{\langle j\rangle}\frac{\partial(\delta\overline{u}^a)}{\partial X^B}dVdY$$

where

$$\mathcal{D}^\beta_{\langle k\rangle ab} = -\frac{\partial^2\tilde{\Psi}}{\partial q^a_{\langle k\rangle}\partial F^{Lb}_{.\beta}}$$

$$\mathcal{H}_{\langle jk\rangle ab} = \frac{\partial^2\tilde{\Psi}}{\partial q^a_{\langle k\rangle}\partial q^b_{\langle j\rangle}}$$

$$\overline{\mathcal{D}}^B_{\langle j\rangle ba} = J^{P-1}F^{P-1B}_{.\alpha}\mathcal{D}^\alpha_{\langle j\rangle ba}$$

$$\hat{\square}^{\alpha\beta}_{ab} = \frac{\partial^2\tilde{\Psi}}{\partial F^{La}_{.\alpha}\partial F^{Lb}_{.\beta}}$$

$$\overline{\square}^{AB}_{ba} = J^{P-1}F^{P-1B}_{.\alpha}\hat{\square}^{\beta\alpha}_{ba}F^{P-1A}_{.\beta}$$
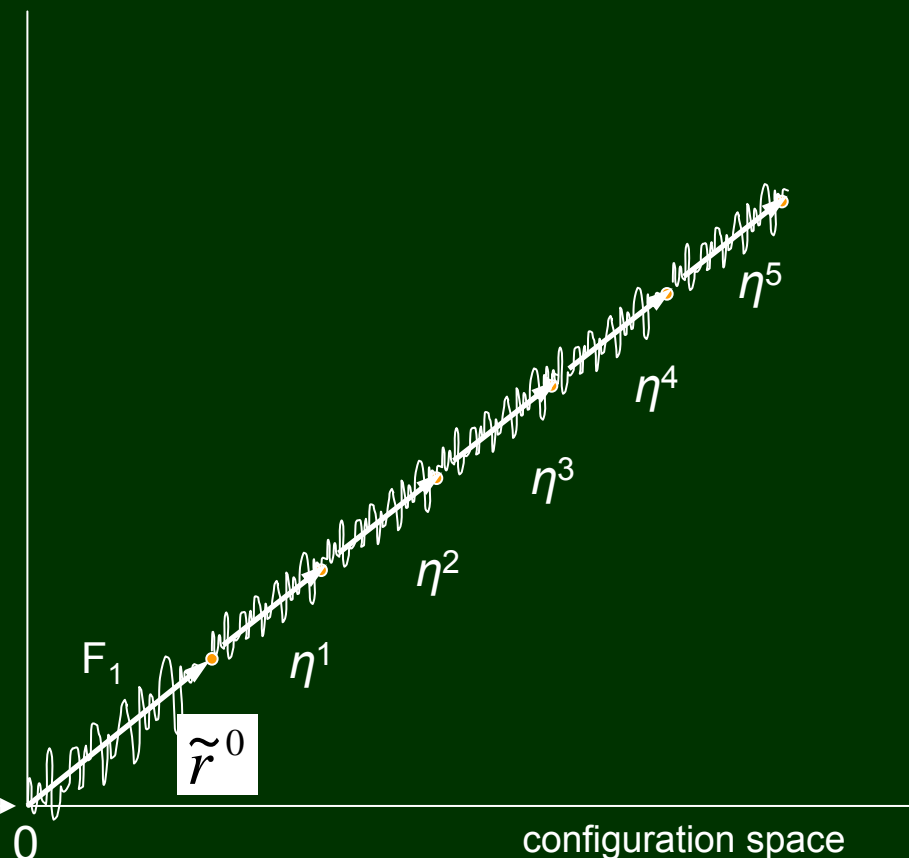
New computational method for global energy minimization

- **Incremental, iterative quasi-static formulation (longer time scales)**
- **Reduce full relaxation problem of atom DOFs to single parameter line search with bisection (predict structure of defect cores without molecular dynamics)**
- **Comparable overall cost (DOF, solution time) to lattice statics**

$$\mathbf{r}_{\langle a\backslash b\rangle} = \overline{\mathbf{F}}^{\mathbf{L}}\tilde{\mathbf{R}}_{\langle a\backslash b\rangle} + \tilde{\mathbf{v}}_{\langle b\rangle} - \tilde{\mathbf{v}}_{\langle a\rangle} = \overline{\mathbf{F}}^{\mathbf{L}}\tilde{\mathbf{R}}_{\langle a\backslash b\rangle} + \tilde{\mathbf{r}}_{\langle a\backslash b\rangle}$$

Cauchy-Born rule   correction

$$\mathbf{r}_{\langle a\backslash b\rangle}^{n+1} = \overline{\mathbf{F}}^{L\,n+1}\tilde{\mathbf{R}}_{\langle a\backslash b\rangle} + \tilde{\mathbf{r}}_{\langle a\backslash b\rangle}^{n+1}$$

$$= \overline{\mathbf{F}}^{L\,n+1}\tilde{\mathbf{R}}_{\langle a\backslash b\rangle} + \eta^{n+1}\tilde{\mathbf{r}}_{\langle a\backslash b\rangle}^{n}$$

$$\mathbf{r}_{\langle a\backslash b\rangle}^{n+m} = \overline{\mathbf{F}}^{L\,n+m}\tilde{\mathbf{R}}_{\langle a\backslash b\rangle} + \eta^{n+m}\tilde{\mathbf{r}}_{\langle a\backslash b\rangle}^{n}$$

η^5

η^4

η^3

η^2

η^1

F_1

$\tilde{r}^0$

Created Model

0   configuration space

Numerical examples

Tungsten with Embedded Atom Method: unit cell calculations for effective properties

- **Point vacancy**
- **Screw dislocation**
- **Low angle grain boundary (twist disclination)**
- **Screw dislocation with plastic shear kinematics**
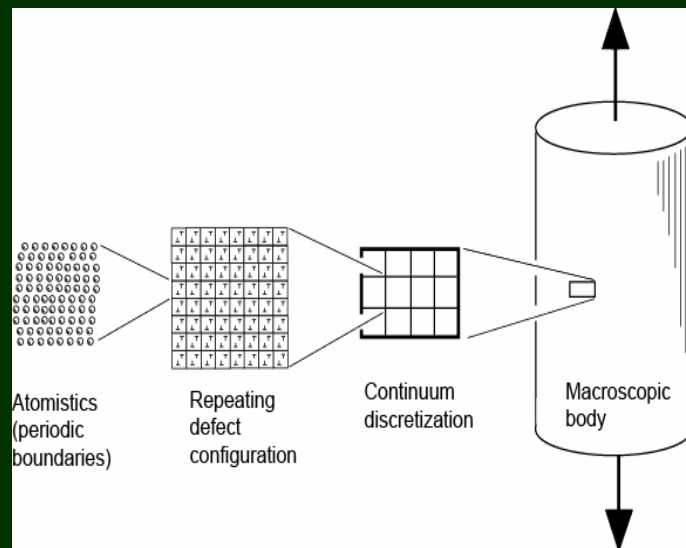
Multiscale Concept
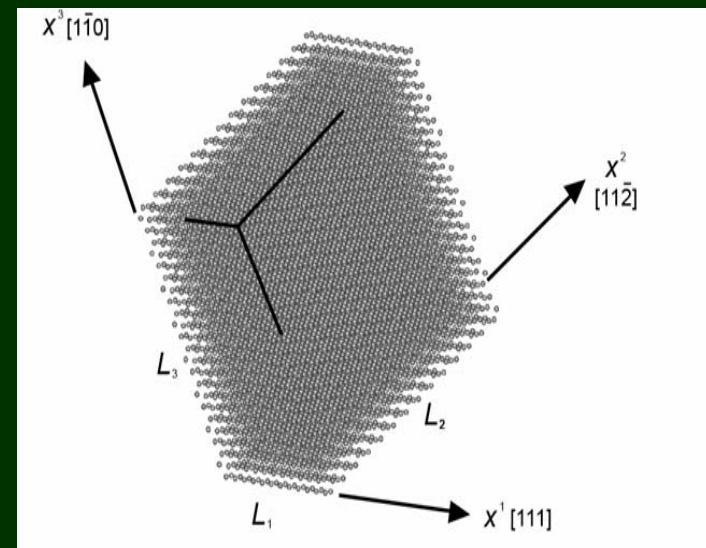
BCC Unit Cell

Atomistic potential for BCC tungsten

$$\tilde{E} = \tilde{E}_N + \tilde{E}_P$$

M.W. Finnis & J.E. Sinclair, *Phil. Mag. A*, Vol. 50, 1984

$$\tilde{E}_P = \frac{1}{2}\sum_{i,j,i\neq j}\tilde{\psi}\left(r_{\langle i\backslash j\rangle}\right)$$

**pair potential
repulsive core interactions**

$$\tilde{E}_N = -A\sum_{\langle i\rangle} f\left(\tilde{\rho}_{\langle i\rangle}\right)$$

**bonding term
cohesive forces**

$$\tilde{\psi}(r) = \begin{cases}(r-c)^2\left(c_0 + c_1 r + c_2 r^2\right) & r \le c \\ 0 & r > c\end{cases}$$

$$f\left(\tilde{\rho}_{\langle i\rangle}\right) = \sqrt{\tilde{\rho}_{\langle i\rangle}}$$

$$r_{\langle i\backslash j\rangle} = \left|\mathbf{r}_{\langle i\backslash j\rangle}\right| = \left|\mathbf{z}_{\langle j\rangle} - \mathbf{z}_{\langle i\rangle}\right|$$

$$\tilde{\phi}(r) = \begin{cases}(r-d)^2 & r \le d \\ 0 & r > d\end{cases}$$

$$\tilde{\rho}_{\langle i\rangle} = \sum_j \tilde{\phi}\left(r_{\langle i\backslash j\rangle}\right)$$

Implementation in homogenization scheme (analytical derivatives and chain rule)

Analytical derivatives
substituted into equilibrium
equation:

$$\mathcal{D}^{\beta}_{\langle j\rangle ab}\frac{\partial \overline{u}^b}{\partial X^A}F^{P-1A}_{.\beta} = \mathcal{H}_{\langle jk\rangle ab}\tilde{v}^b_{\langle k\rangle}$$

**Potential used by Vitek [1998] and others for dislocation core structures in W,
but has drawbacks for atoms too tightly packed [Ackland & Thetford, *Phil. Mag. A*, 1987].**

Vacancy – [100] tension

Defect Configuration

Numerical Validation

Legend:
- Homogenization, $\rho^d = 5.0(10)^{-4}$
- Conjugate gradient, $\rho^d = 5.0(10)^{-4}$
- Homogenization, $\rho^d = 1.2(10)^{-4}$
- Conjugate gradient, $\rho^d = 1.2(10)^{-4}$
- Homogenization, $\rho^d = 5.5(10)^{-5}$
- Conjugate gradient, $\rho^d = 5.5(10)^{-5}$
- Homogenization, $\rho^d = 3.1(10)^{-5}$
- Conjugate gradient, $\rho^d = 3.1(10)^{-5}$
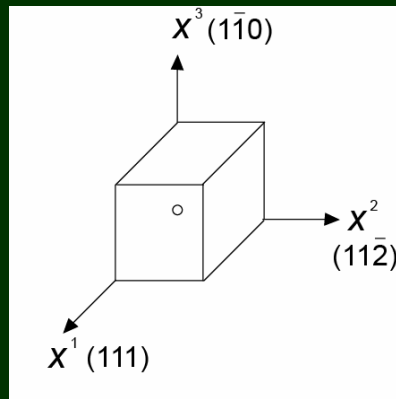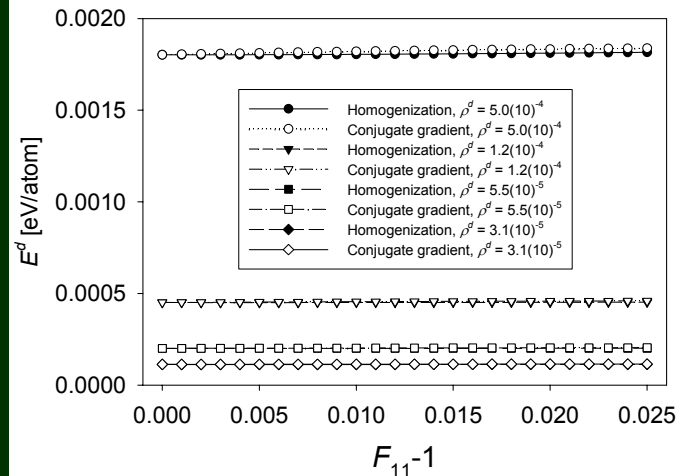
Remarks

- Minimum energy configurations comparable

- Energy compares with experimental result of 3.6 eV [Schultz, 1991]

- Stiffness affected little by low defect concentration

- Strong deformation-induced anisotropy, could be artifact of EAM potential

Defect Energy
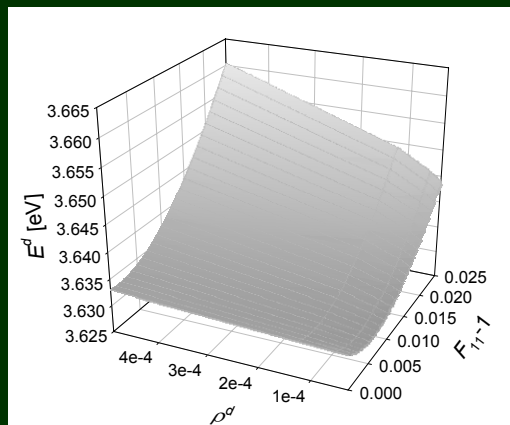
Elastic Stiffness
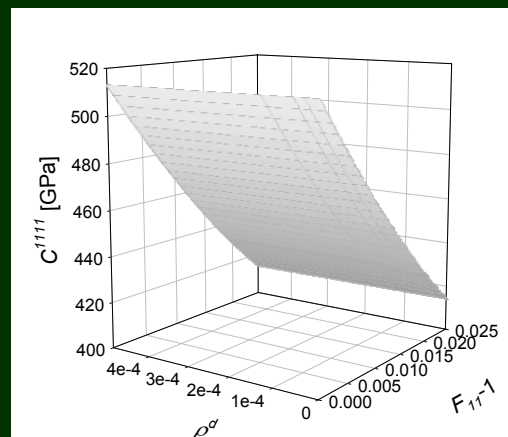
Zener Anisotropy
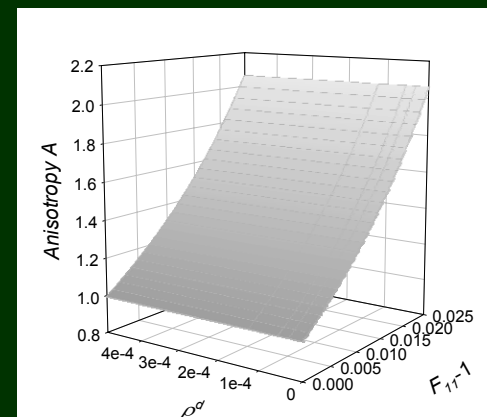
Screw dislocation configuration

[111](1 $\overline{1}$0) screw dislocation in BCC tungsten
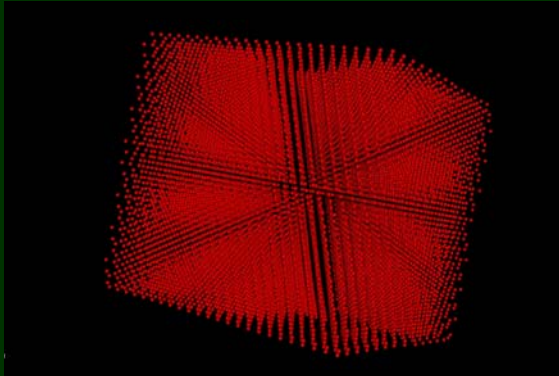
unit cell, 32256 atoms
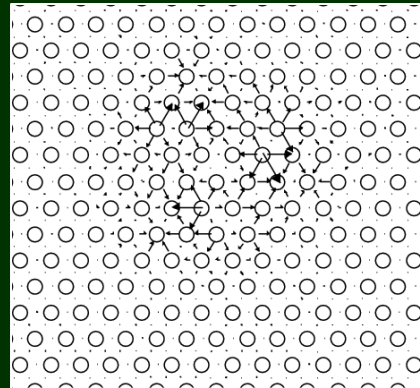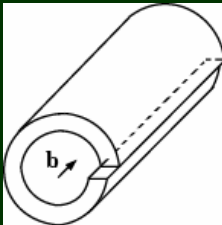
-screw dislocation core
-relative (111)-displacements to perfect BCC lattice
-null applied displacements
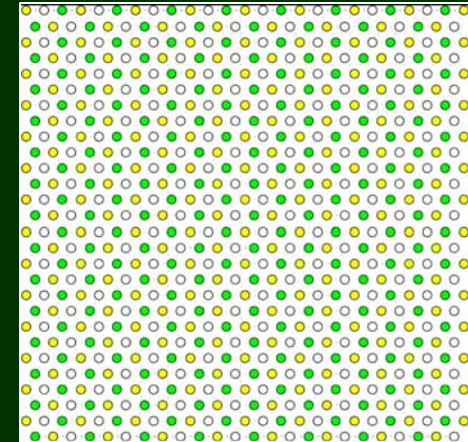
-screw dislocation core
-relative (111) displacements to initial lattice with defect
-111-compression (movie)

-Three-fold symmetry of W dislocation core agrees with lattice statics solution of Vitek [1976, Proc. R. Soc. Lond. A]

-Tension-compression asymmetry of stress & stiffness agrees with experiments

-Results of homogenization method cross-verified using sequential lattice statics (Paradyn code, S. Plimpton)

Undeformed mechanical properties: W unit cells with periodic dislocations

Isolated screw
(lattice curvature)
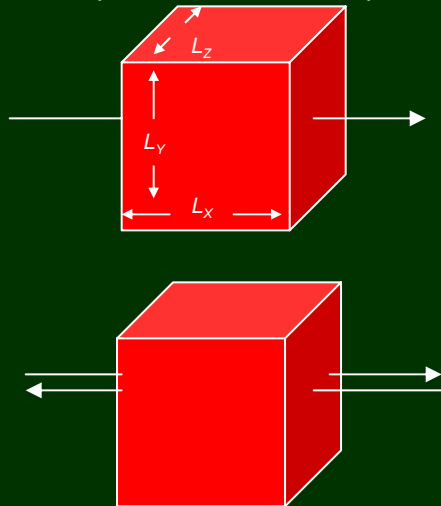
Screw dipole
(counteracting Burgers vectors)

$[1\bar{1}0]$

$[11\bar{2}]$

$[111]$

Elastic constants: single dislocation

C^{1111}
C^{1122}
C^{1212}

$C^{a\alpha b\beta}$ [GPa]

ρ_d [1/nm^2]

Zener anisotropy factor

$A = 2C^{1212}/(C^{1111}-C^{1122})$

Single dislocation
Dislocation dipole

ρ_d [1/nm^2]

Elastic constants: dislocation dipole

C^{1111}
C^{1122}
C^{1212}

$C^{a\alpha b\beta}$ [GPa]

ρ_d [1/nm^2]

Total energy per atom

e [ev/atom]

Single dislocation
Dislocation dipole

ρ_d [1/nm^2]
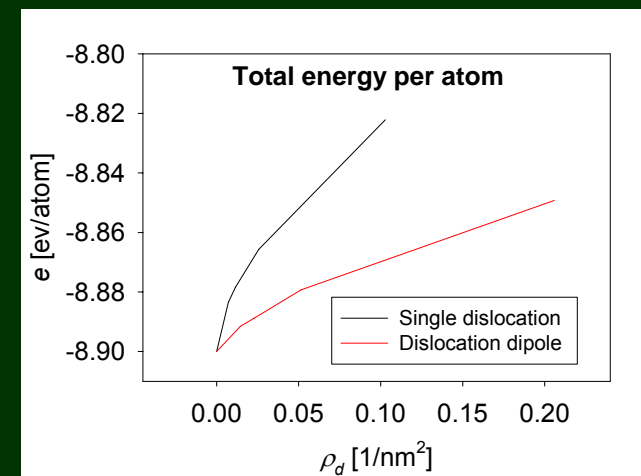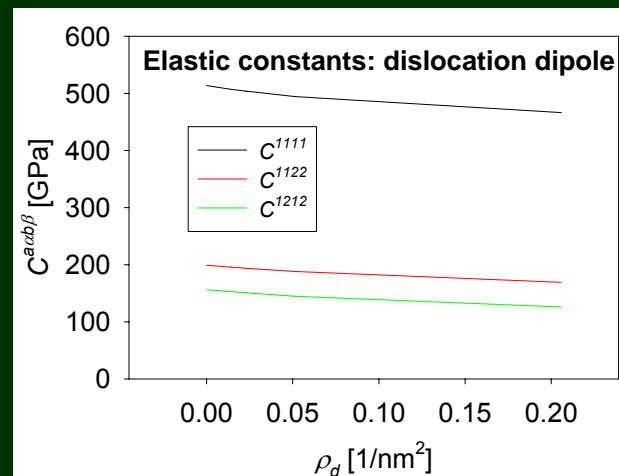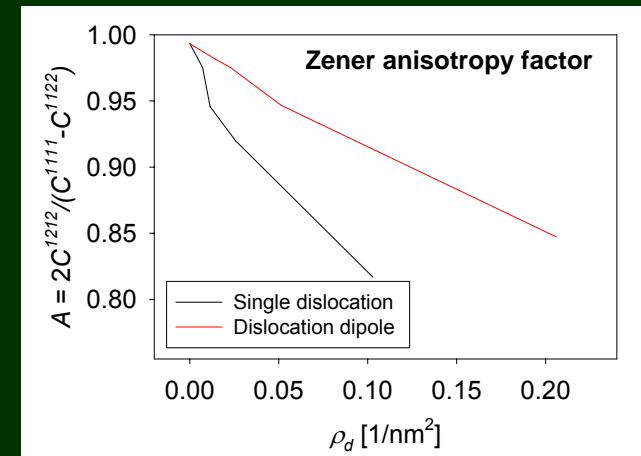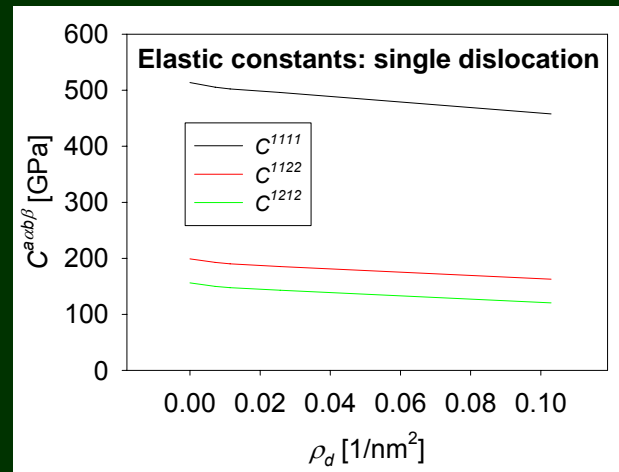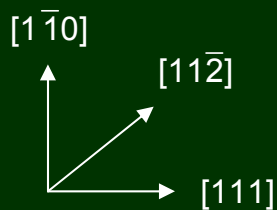
Screw dislocation with elastic shear

28800 atom simulation
BCC Tungsten
[111] Screw dislocation
1% elastic shear strain imposed
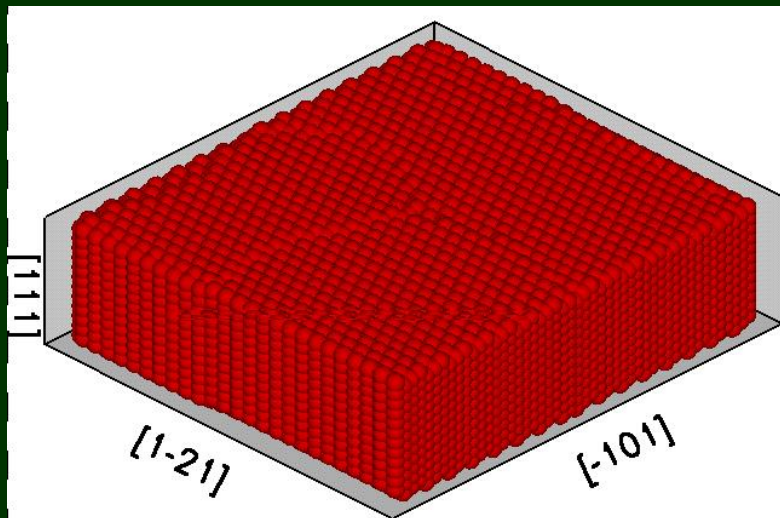
Relaxed atomic coordinates
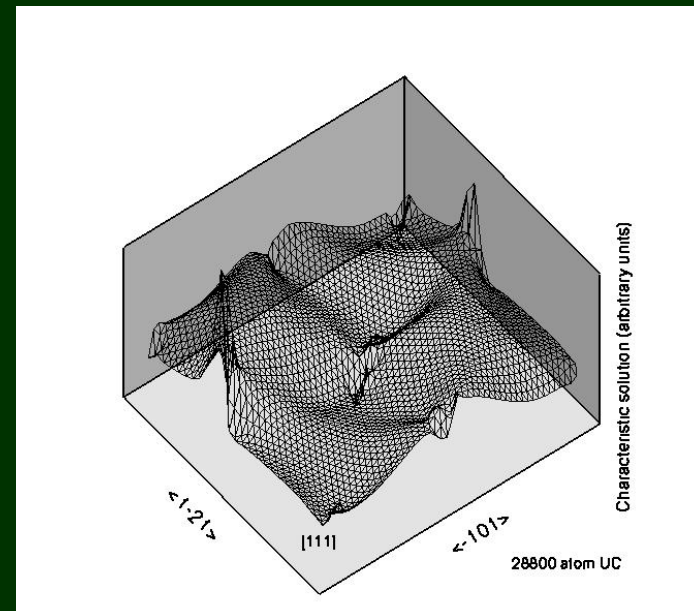
Scaled asymptotic correction $v_{<k>}$

Screw dislocation – [111] tension

Defect Configuration

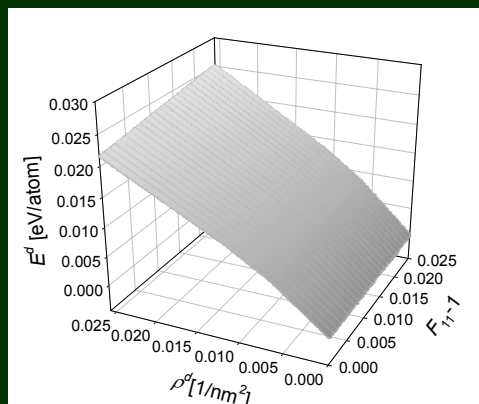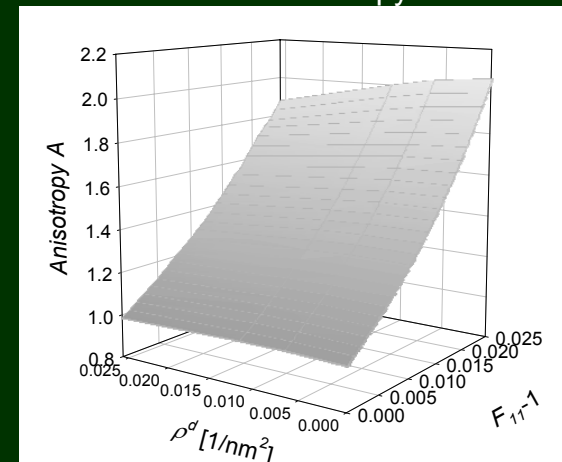Numerical Validation

Defect Energy

Elastic Stiffness
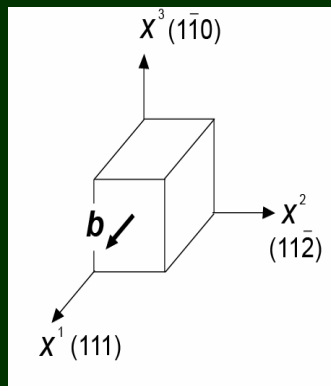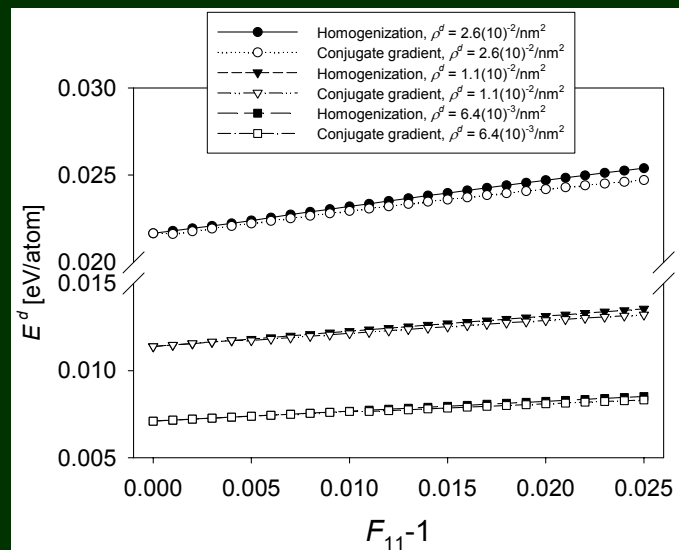
Zener Anisotropy

Remarks:

- Comparable minimum energy configurations attained with different methods
- Positive coupling of defect energy and stretch
- Stiffness and anisotropy affected by dislocations , agrees with experimental trends for Cu [Smith, 1953, *Phil. Mag. A*]
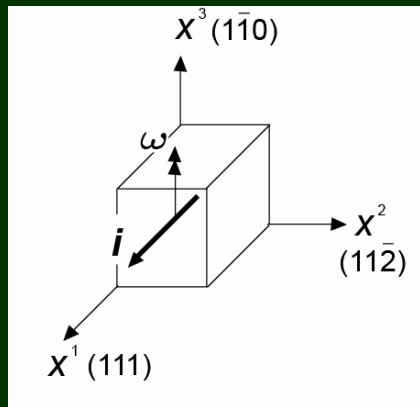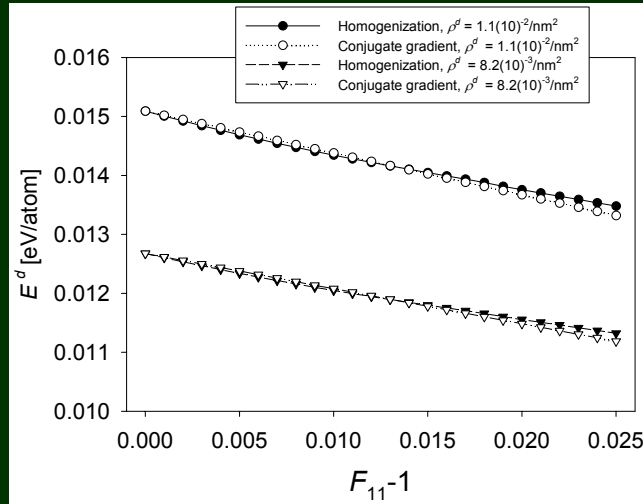- Large defect densities: ~10 nm spacing
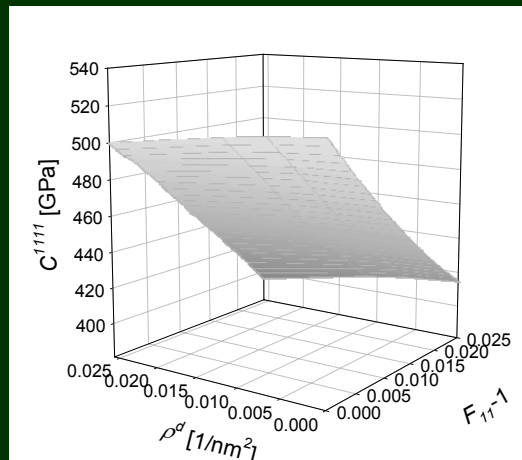
0.2-radian twist boundary: [111]-tension
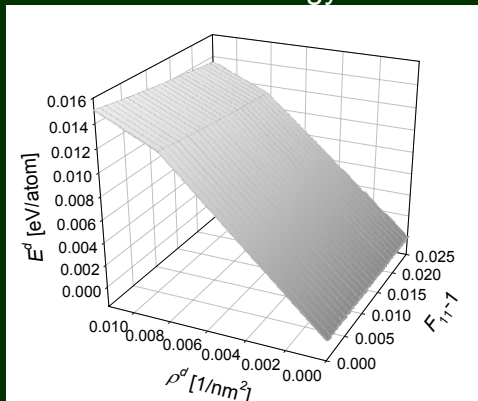
Defect Configuration
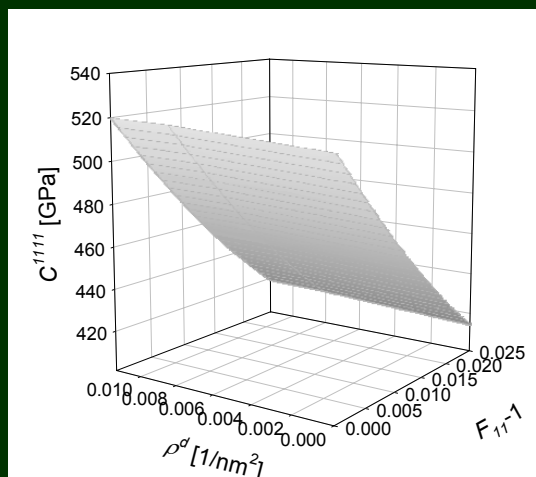

Numerical Validation

Remarks:

- Comparable minimum energy configurations attained with homogenization method and with conjugate gradient technique

- *Negative* coupling of defect energy and applied stretch

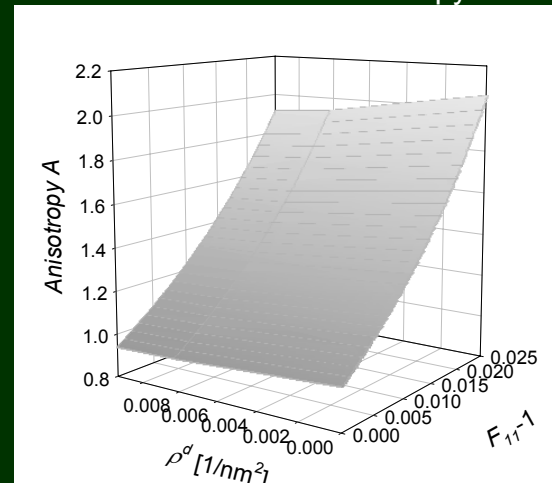- Stiffness and anisotropy affected significantly by twist boundary
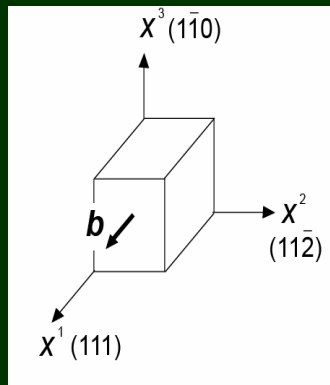
Defect Energy

Elastic Stiffness

Zener Anisotropy

Fixed screw dislocation (atoms) superimposed [110]-glide (continuum)

Defect Configuration

X^3 ($1\bar{1}0$)

X^2 ($11\bar{2}$)

b

X^1 (111)

Elastic-plastic kinematics, pure shear:

$$[F] = \begin{bmatrix} 1 & 0 & \gamma \\ 0 & 1 & 0 \\ 0 & 0 & 1 \end{bmatrix} = \begin{bmatrix} 1 & 0 & (\gamma^L + \gamma^P) \\ 0 & 1 & 0 \\ 0 & 0 & 1 \end{bmatrix}$$
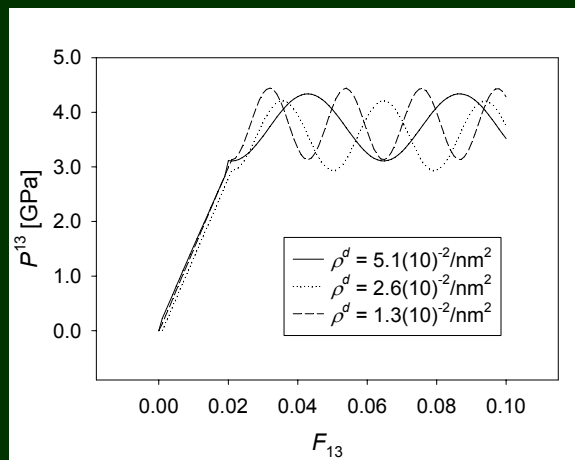
Remarks:

-Peierls-like oscillations depend on size α^{-1} of unit cell (controlled by distance traveled by dislocation)

-Elastic stiffness and energy changes from atomistics reflected in plasticity simulation

Plasticity kinetics:

$$\gamma^P = \begin{cases} 0 & \forall \gamma \leq \gamma_0^y \\ \gamma - \gamma_0^y - \dfrac{\gamma_1^y}{2}\left\{1 + \sin\left[(2\pi/\alpha b)(\gamma - \gamma_0^y - \alpha b/4)\right]\right\} & \forall \gamma \geq \gamma_0^y \end{cases}$$
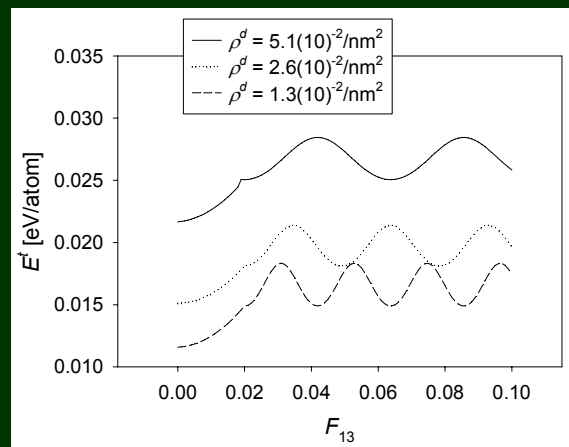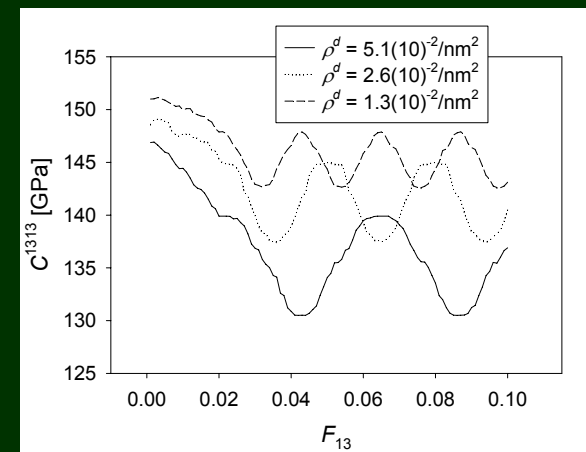
Resolved Shear Stress

P^{13} [GPa] vs F_{13}

- $\rho^d = 5.1(10)^{-2}/nm^2$
- $\rho^d = 2.6(10)^{-2}/nm^2$
- $\rho^d = 1.3(10)^{-2}/nm^2$

Elastic + Defect Energy

E^t [eV/atom] vs F_{13}

- $\rho^d = 5.1(10)^{-2}/nm^2$
- $\rho^d = 2.6(10)^{-2}/nm^2$
- $\rho^d = 1.3(10)^{-2}/nm^2$

Elastic Stiffness

C^{1313} [GPa] vs F_{13}

- $\rho^d = 5.1(10)^{-2}/nm^2$
- $\rho^d = 2.6(10)^{-2}/nm^2$
- $\rho^d = 1.3(10)^{-2}/nm^2$

Summary

- **<u>Key aspects of multiscale theory</u>**
    - Finite deformation with evolving intermediate configuration
    - Born correction (atoms) linked to fine scale asymptotic solution (continuum)
    - Separate but co-linear coordinate systems at each scale
    - No need to match boundary interfaces as in some other multiscale methods
    - Presently restricted to periodic defect distributions at each macro-element

- **<u>Implementation and examples</u>**
    - Accurate alternative to conjugate gradient minimization
    - Convergence and performance properties not fully explored
    - Demonstrated effects of large defect concentrations on moduli & energy of W
    - Static formulation, unable to predict plasticity kinetics from atomic scale, but should be possible in future with dynamic formulation
    - Incorporates plasticity kinematics and continuum-type slip
    - Mixed domains like quasi-continuum [Tadmor, Ortiz, Shenoy et al.] possible